Recovering lost 21-cm radial modes for cross correlation with the CMB and photo-z galaxies via cosmic tidal reconstruction

Hong-Ming Zhu,[1, 2, 3, *] Ue-Li Pen,[4, 5, 6, 7] Yu Yu,[8] and Xuelei Chen[1, 2, 9]

[1]*Key Laboratory for Computational Astrophysics, National Astronomical Observatories,*
Chinese Academy of Sciences, 20A Datun Road, Beijing 100012, China
[2]*University of Chinese Academy of Sciences, Beijing 100049, China*
[3]*Berkeley Center for Cosmological Physics and Department of Physics,*
University of California, Berkeley, California 94720, USA
[4]*Canadian Institute for Theoretical Astrophysics, University of Toronto,*
60 St. George Street, Toronto, Ontario M5S 3H8, Canada
[5]*Dunlap Institute for Astronomy and Astrophysics, University of Toronto,*
50 St. George Street, Toronto, Ontario M5S 3H4, Canada
[6]*Canadian Institute for Advanced Research, CIFAR Program in*
Gravitation and Cosmology, Toronto, Ontario M5G 1Z8, Canada
[7]*Perimeter Institute for Theoretical Physics, 31 Caroline Street North, Waterloo, Ontario, N2L 2Y5, Canada*
[8]*Department of Astronomy, Shanghai Jiao Tong University, 800 Dongchuan Road, Shanghai 200240, China*
[9]*Center of High Energy Physics, Peking University, Beijing 100871, China*
(Dated: February 21, 2018)

21-cm intensity mapping has emerged as a promising technique to map the large-scale structure of the Universe, at redshifts z from 1 to 10. Unfortunately, many of the key cross correlations with the cosmic microwave background and photo-z galaxies have been thought to be impossible due to foreground contamination for radial modes with small wave numbers. In this paper, we apply tidal reconstruction to the simulated 21-cm fields and recover the lost large-scale radial modes successfully. We estimate the detectabilities of the cross correlation signals and find them can be detected at high significance. The tidal field reconstruction method opens up a new set of possibilities to probe the Universe and is extremely valuable not only for 21-cm surveys but also for cosmic microwave background and photometric redshift observations.

I. INTRODUCTION

The current and future cosmic surveys aim to map a large fraction of the Universe with unprecedented precision by observing the large-scale structure (e.g. SDSS [1], DES [2], PFS [3], DESI [4], LSST [5], Euclid [6]) and the cosmic microwave background (CMB) (e.g. Planck [7], SPT-3G [8], Advanced ACTPol [9], CMB-S4 [10]). Precision measurements of cosmological parameters from the autocorrelations of large-scale structure and CMB observations and the cross correlations between different observations can improve constraints on the properties of dark energy, modifications to general relativity, neutrino masses, and primordial non-Gaussianities substantially. In addition to these observation methods, 21-cm intensity mapping has emerged as a powerful method to map the large-scale structure of the Universe [11–13]. Instead of resolving millions of individual galaxies, the 21-cm intensity mapping technique measures the large-scale structure by detecting the aggregate 21-cm emission of neutral hydrogen from many galaxies in large voxels. The redshifted 21-cm emission line which provides the redshift information can be resolved exquisitely in the frequency domain. Therefore, this allows radio telescopes to conduct rapid and efficient surveys of large volumes of the Universe. The ongoing and upcoming 21-cm surveys including CHIME [14], HIRAX [15], Tianlai [16], BINGO [17], FAST [18], MeerKAT [19], and SKA [20] can improve the baryon acoustic oscillations (BAO) measurements by observing a larger cosmic volume at higher redshifts compared to current galaxy surveys.

The primary challenge for 21-cm intensity mapping experiments is the presence of the astrophysical foregrounds from galactic and extra-galactic synchrotron emissions, which are three orders of magnitude brighter than the cosmological 21-cm signals. The synchrotron foregrounds are known to be spectrally smooth in the frequency domain where the redshifted 21-cm signals from different redshifts fluctuate at different frequencies. In principle, the foregrounds only impact the long wavelength density fluctuations along the line of sight, i.e., the modes with small $k_\parallel$ in Fourier space [21, 22]. However, the instrumental effects (e.g. spectral response, calibration, etc) further lead to an unsmooth foreground component, often referred as the foreground wedge at the low $k_\parallel$ and high $k_\perp$ area in Fourier space [23–27]. The synchrotron foregrounds can be cleaned by exploiting their smooth spectral structure [28–31]. As demonstrated in Ref. [31], the foregrounds can be cleaned well below the foreground wedge with the precise calibration of the instrument, leaving only $k_\parallel < 0.02\ h\mathrm{Mpc}^{-1}$ modes unaccessible.

However, while there are not many Fourier modes at $k_\parallel < 0.02\ h\mathrm{Mpc}^{-1}$, many other cosmological observations such as weak lensing, photometric-redshift galaxies, and integrated Sachs-Wolf (ISW) effect can only probe

these modes. These observations involve a broad window function along the line of sight and measure the projected modes, i.e., the modes with small $k_\parallel$, which are all contaminated by the foreground emissions in 21-cm intensity mapping observations. Therefore, the proposed cross correlation of 21-cm intensity mapping with weak gravitational lensing [32–34], photo-z galaxies [32, 35–39], and ISW effect [38] would be severely degraded in the presence of foregrounds. Recovering the lost large-scale radial modes for cross correlations is thus crucial in order to fully exploit the 21-cm intensity mapping experiments. The cross-correlation measurements will benefit other observations as well, since the cross correlations are expected to be more robust to the systematics than auto-correlations from individual experiments. It also enables the use of sample variance cancellation technique [40] to measure cosmological parameters [35–37].

Recently a new method called cosmic tidal reconstruction has been developed [41, 42]. The small-scale density fluctuations are significantly affected by the large-scale density field as a consquence of nonlinear mode coulping. The large-scale tidal shear field causes anisotropic distortions of the locally measured small-scale matter power spectrum. Such local anisotropic tidal distortions can be exploited to reconstruct the large-scale tidal shear and hence density fields. The reconstruction of gravitational tidal shear from local small-scale matter power spectrum is described by the same formulation as the reconstruction of gravitational lensing induced shear. As shown in Ref. [42], the density modes with small $k_\parallel$ and large $k_\perp$ are well reconstructed, with cross-correlation coefficient close to 1 for reconstruction with the full dark matter density field. These reconstructed density modes are exactly those lost in the foreground subtraction of 21-cm experiments. The tidal reconstruction technique enables the reconstruction of lost 21-cm radial modes, which provides important radial information essential for cross correlating with the CMB and photometric observations.

In this paper, we apply cosmic tidal reconstruction to the simulated 21-cm field with low $k_\parallel$ foreground modes subtracted. The small $k_\parallel$ radial modes are recovered successfully after tidal reconstruction. Then we cross correlate the reconstructed 21-cm field with the simulated CMB lensing, photo-z galaxy and ISW effect fields and estimate the detectability of the cross-correlation signals with the current 21-cm experiments. The tidal field reconstruction method provides us a new way to study the large-scale matter distribution in the Universe through cross correlations and has profound implications for the current and future 21-cm experiments.

The paper is organized as follows. In Sec. II, we introduce the cosmic tidal reconstruction. In Sec. III, we apply tidal field reconstruction to the simulated foreground subtracted 21-cm density field and shows the reconstruction results. Section IV shows the cross-correlation signal recovered after reconstruction and estimates the detectability with current 21-cm experiments. We discuss further improvements and future applications in Sec. V

and conclude in Sec. **??**.

II. COSMIC TIDAL RECONSTRUCTION

The large-scale density field can be reconstructed accurately from the anisotropic tidal distortions of the locally-measured matter power spectrum [41, 42]. The basic idea of purely transverse tidal reconstruction has been proposed in Ref. [41] and further expanded in Ref. [42]. In this section, we briefly discuss the physical idea and outline the operational procedure of the tidal field reconstruction. More details of this reconstruction method are presented in Ref. [42].

A. Cosmic tides

The evolution of small-scale density perturbations is modulated by long wavelength perturbations during nonlinear structure formation. The gravitational coupling of a long wavelength tidal field with small-scale density fluctuations has been studied extensively [43]. The leading-order observable of a long wavelength density perturbation on small-scale density perturbations is described by the large-scale tidal field,

$$t_{ij} = \Phi_{L,ij} - \delta_{ij}\Phi_{L,kk}/3, \qquad (1)$$

where Φ_L is the long wavelength gravitational potential sourced by the long wavelength density perturbation δ_L. Here $\Phi_{L,ij}$ denotes partial derivatives of Φ_L to x^i and x^j. Note that we have projected out the trace of $\Phi_{L,ij}$, which corresponds to the local mean density. Since the change of shape is more robust than the change of number density, we shall focus on the gravitational tidal shear, i.e., the traceless tidal field. The locally observed matter power spectrum in the presence of the large-scale tidal field t_{ij} can be calculated using Lagrangian perturbation theory and is given by

$$P(\boldsymbol{k},\tau)|_{t_{ij}} = P(k,\tau) + \hat{k}^i\hat{k}^j t_{ij}^{(0)} P(k,\tau) f(k,\tau), \qquad (2)$$

where τ is the conformal time, $P(k,\tau)$ is the isotropic linear power spectrum, $\hat{\boldsymbol{k}}$ is the unit vector, the superscript (0) denotes the initial time defined in perturbation calculation. The coupling of the large-scale tidal field to small-scale density fluctuations is described by the tidal coupling coefficient

$$f(k,\tau) = 2\alpha(\tau) - \beta(\tau)\frac{d\ln P(k,\tau)}{d\ln k}, \qquad (3)$$

where $\alpha(\tau)$ and $\beta(\tau)$ are integrals involving background cosmological parameters and can be computed numerically [42, 43]. The above result only includes the leading order effect of the coupling between the large-scale tidal field and small-scale density fluctuations. In reality the

density field is quite nonlinear and involves all higher order interactions. The reconstructed density field would be biased when the theoretical description of the nonlinear coupling in the above equation is not accurate. This problem can be addressed using the transfer function calibriated from simulations [42].

The traceless tidal tensor t_{ij} can be decomposed into five independently observable components $(\gamma_1, \gamma_2, \gamma_x, \gamma_y, \gamma_z)$ [42]. We notice that the two transverse shear terms,

$$\gamma_1 = (\Phi_{L,11} - \Phi_{L,22})/2, \ \gamma_2 = \Phi_{L,12}, \qquad (4)$$

which describe quadrupolar distortions in the tangential plane perpendicular to the line of sight, are less affected by peculiar velocities. Thus, in the following computation we shall use them to perform reconstruction. Once we have the tidal shear terms γ_1 and γ_2, the reconstructed density field can be obtained by

$$\delta_r(\boldsymbol{k}) = \frac{Ak^2}{(k_1^2 + k_2^2)^2} \left[(k_1^2 - k_2^2)\gamma_1(\boldsymbol{k}) + 2k_1k_2\gamma_2(\boldsymbol{k}) \right], \ (5)$$

where A is the normalization coefficient. Since we only use two transverse tidal shear fields γ_1 and γ_2 for reconstruction, the change of the large-scale density field along the line of sight is inferred from the variations of γ_1 and γ_2 along the z-axis. The noise for the reconstructed density field is anisotropic in Fourier space. The tidal reconstruction technique works best for modes in the high $k_\perp$ and low $k_\parallel$ region, which can not be obtained from 21-cm surveys directly but contribute substantially to observables from other cosmological observations as discussed above. Cosmic tidal reconstruction provides a new possible way to recover the lost radial modes and to improve the cross-correlation signals.

B. Reconstruction algorithm

In this subsection, we describe the tidal reconstruction method used in the next section.

1. Reducing nonlinearities

The first step is to smooth the nonlinear density field with a Gaussian kernel,

$$\delta_R(\boldsymbol{k}) = W_R(\boldsymbol{k})\delta(\boldsymbol{k}), \qquad (6)$$

where

$$W_R(\boldsymbol{k}) = \exp(-k^2 R^2/2), \qquad (7)$$

which filters out small-scale structures. The perturbative description of tidal coupling in Eq. (2) is not valid in the strong non-Gaussian regions. We need to smooth small-scale nonlinear structures to reduce nonlinearities. Here, we take $R = 1.25$ Mpc/h, which is close to the optimal filter scale as demonstrated in Refs. [41, 42].

The second step is to gaussianize the smoothed density field by taking a logarithmic transform or mapping the density fluctuations into a Gaussian distribution according to their density values. We shall use the latter method since after the simulated 21-cm foreground subtraction process, some of the density contrasts become smaller than -1, which makes it hard to take the logarithmic transform, $\ln(1 + \delta)$.

2. Estimating tidal shear fields

The coupling of the large-scale tidal field and small-scale density fluctuations leads to a local anisotropy of quadratic statistics. The tidal shear fields can be reconstructed by applying qudratic estimators to the Gaussianized density field δ_g as

$$\hat{\gamma}_1(\boldsymbol{x}) = \left[\delta_g^{w_1}(\boldsymbol{x})\delta_g^{w_1}(\boldsymbol{x}) + \delta_g^{w_2}(\boldsymbol{x})\delta_g^{w_2}(\boldsymbol{x}) \right]/2,$$
$$\hat{\gamma}_2(\boldsymbol{x}) = \left[\delta_g^{w_1}(\boldsymbol{x})\delta_g^{w_2}(\boldsymbol{x}) \right], \qquad (8)$$

where

$$\delta_g^{w_1}(\boldsymbol{k}) = i\hat{k}_1 w(\boldsymbol{k})\delta_g(\boldsymbol{k}), \ \delta_g^{w_2}(\boldsymbol{k}) = i\hat{k}_2 w(\boldsymbol{k})\delta_g(\boldsymbol{k}), \quad (9)$$

and the filter is

$$w(\boldsymbol{k}) = \frac{\sqrt{P(\boldsymbol{k})f(\boldsymbol{k})}}{P_{\text{tot}}(\boldsymbol{k})}, \qquad (10)$$

Here, $P_{\text{tot}}(\boldsymbol{k})$ is the total power spectrum of the 21-cm density field which includes both the signal and noise. The reconstruction of tidal shear fields is similar to the reconstruction of lensing shear fields from 21-cm temperature fields. The quadratic estimators presented above can be constructed using either the maximum likelihood method or the inverse variance weighting [44–46].

3. Generating the density field

After we get the tidal shear fields γ_1 and γ_2, the tidal reconstructed density field is given by Eq. (5). In general, the reconstructed field $\delta_r(\boldsymbol{k})$ can be written as

$$\delta_r(\boldsymbol{k}) = C(\boldsymbol{k})\delta(\boldsymbol{k}) + N(\boldsymbol{k}), \qquad (11)$$

where $C(\boldsymbol{k}) = P_{\delta_r\delta}(\boldsymbol{k})/P_\delta(\boldsymbol{k})$, $\delta(\boldsymbol{k})$ is the original matter density field and $N(\boldsymbol{k})$ includes the noises from 21-cm observation and from reconstruction. The factor $C(\boldsymbol{k})$, often referred as the propagator, quantifies how much information of the original density distribution is reconstructed. To get an unbiased measurement of the original density field, we can deconvolve the propagator $C(\boldsymbol{k})$ from the reconstructed field,

$$\hat{\delta}_r = \delta_r(\boldsymbol{k})/C(\boldsymbol{k}) = \delta(\boldsymbol{k}) + N(\boldsymbol{k})/C(\boldsymbol{k}). \qquad (12)$$

This factor can be computed by performing reconstruction with the simulated observation mock data [47–49].

III. IMPLEMENTATION AND RESULTS

To test the performance of reconstruction, we run an ensemble of six N-body simulations with the CUBEP^{3}M code [50]. Each simulation involves 1024^3 dark matter particles in a cubic box of side length 1200 Mpc/h. We use the snapshot at redshift $z = 1$ and generate the dark matter density field on a 1024^3 grid. We could approximately use the dark matter density to represent the 21-cm source distribution, i.e., the neutral hydrogen. This is a good approximation since the neutral hydrogen traces the total mass distribution fairly well at low redshifts (see Refs. [51, 52] for more discussions about the modeling of neutral hygrogen in the Universe).

There are several noises for 21-cm experiments we need to consider to model the observed 21-cm signal from intensity mapping observations, including the astrophysical foreground, the receiver noise, and the shortest baseline for inteferometers.

A detailed 21-cm foreground subtraction simulation is beyond the scope of this paper. Instead we simply use a high-pass filter along the line of sight,

$$W_{\rm fs}(k_\parallel) = 1 - e^{-k_\parallel^2 R_{\rm fs}^2/2}, \qquad (13)$$

which removes the small $k_\parallel$ density modes, to simulate the loss of modes due to foreground contamination. We use the two different foreground scales $R_{\rm fs} = 60$ Mpc/h and 15 Mpc/h in reconstruction, which give $W_{\rm fs} = 0.5$ at $k_\parallel = 0.02$ hMpc^{-1} and 0.08 hMpc^{-1}, respectively. The former is an optimal case, i.e., we only loss modes with $k_\parallel \lesssim 0.02$ hMpc^{-1} [31], while the latter is already achieved in the current 21-cm observations [53, 54].

For 21-cm observations around redshift $z = 1$, the resolution of small-scale structures is mainly determined by the thermal noise. The thermal noise power P_N is about $150 - 600$ (Mpc/h)^3 for a HIRAX-like interferometer, depending on the neutral hydrogen fraction and bias [52]. We assume the experimental noise to be zero above a cut off scale and infinity below this scale. We choose it to be $k_N = 0.6$ hMpc^{-1}, which is about the scale where the thermal noise power dominates over the matter power spectrum. The effect of the experimental noise can be modeled by applying a step function

$$\Theta(k_N - k) = \begin{cases} 1, & k \le k_N \\ 0, & k > k_N \end{cases},$$

to the dark matter density field from the simulation.

Most current 21-cm intensity mapping experiments are carried on interferometers. The largest angular scale can be probed is decided by the shortest baseline of the interferometer. We also using a step function

$$\Theta(\ell - \ell_s) = \begin{cases} 1, & \ell \ge \ell_s \\ 0, & \ell < \ell_s \end{cases},$$

to model this effect, where the largest scale can be probed is $\ell_s = 115$ or $k_\perp = 0.05$ h/Mpc at redshift $z = 1$. This corresponds to a shortest baseline of ~ 7 m.
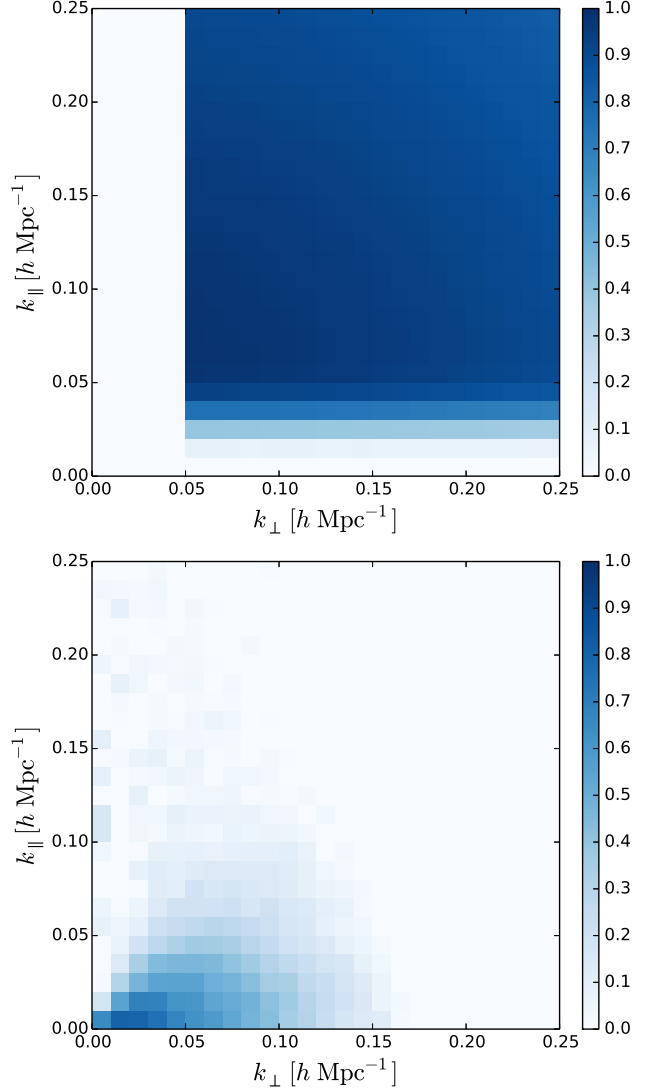

FIG. 1. *Top*: The cross-correlation coefficient of the simulated 21-cm intensity mapping field $\delta_{\rm IM}(\boldsymbol{k})$ with the original full dark matter density field $\delta(\boldsymbol{k})$. *Bottom*: The cross-correlation coefficient of the reconstructed density field $\hat{\delta}_r(\boldsymbol{k})$ with the original full dark matter density field $\delta(\boldsymbol{k})$. These results are for the foreground scale $R_{\rm fs} = 60$ Mpc/h, where modes with $k_\parallel \lesssim 0.02$ hMpc^{-1} are subtracted.

In summary, the simulated 21-cm field from intensity mapping is given by

$$\delta_{\rm IM}(\boldsymbol{k}) = \delta(\boldsymbol{k})W_{\rm fs}(k_\parallel)\Theta(k_N - k)\Theta(\ell - \ell_s), \qquad (14)$$

where $\delta(\boldsymbol{k})$ is the full density field from the simulation. We apply tidal reconstruction to the simulated 21-cm field and get the reconstructed density field defined in Eq. (12) using the algorithm described above.

Figure 1 shows the two-dimensional cross-correlation coefficient of the 21-cm intensity mapping field with the full dark matter density field. We also plot the cross-correlation coefficient of the reconstructed density field with the full dark matter density field. These re-
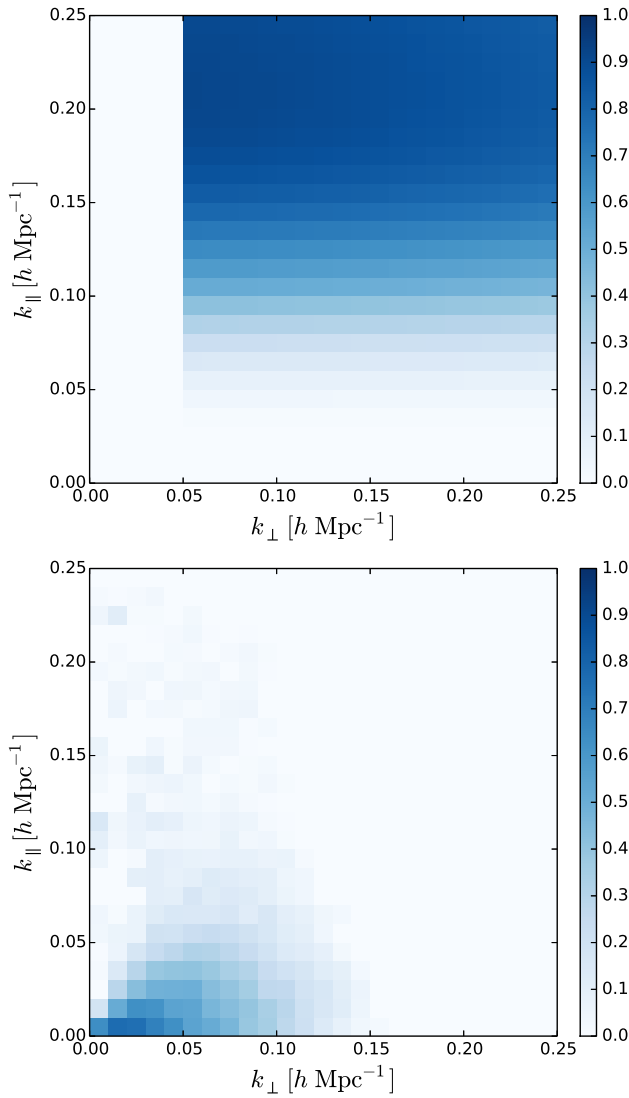
FIG. 2. Same as Fig. 1, but for the foreground scale $R_{\rm fs} = 15$ Mpc$/h$, where modes with $k_\parallel \lesssim 0.08$ hMpc^{-1} are subtracted.
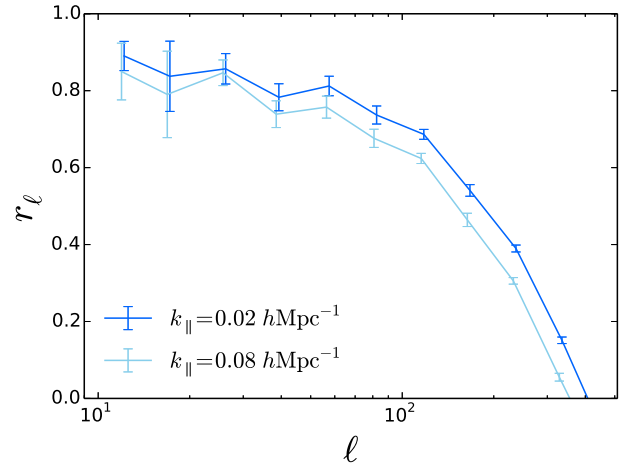

FIG. 3. The cross-correlation coefficients of the projected full dark matter density field with the projected reconstructed density fields for the foreground scales $k_\parallel = 0.02$ hMpc^{-1} and 0.08 hMpc^{-1}. The angular scale ℓ is related to the three-dimensional wave number k through $\ell = k\chi(z = 1)$, where $\chi(z = 1) = 2301$ Mpc$/h$ is the comoving distance to redshift $z = 1$. The cross-correlation coefficient is larger than 0.7 and 0.65 at scale $\ell \lesssim 100$ for the small $k_\parallel$ and large $k_\parallel$ foreground scales. The error bars are estimated using the bootstrap re-sampling method.

sults are for the foreground scale $R_{\rm fs} = 60$ Mpc$/h$, i.e., $k_\parallel = 0.02$ hMpc^{-1}. The lost large-scale radial modes are successfully recovered by tidal reconstruction. Figure 2 shows the corresponding results for the foreground scale $R_{\rm fs} = 15$ Mpc$/h$, i.e., $k_\parallel = 0.08$ hMpc^{-1}. We note that the loss of more large-scale radial modes does not degrade the performance of reconstruction significantly. This is because the tidal reconstruction method uses small-scale structure to reconstruct the large-scale density field and the reconstruction performance mainly depends on the number of small-scale modes.

To clearly see how well the $k_\parallel \sim 0$ modes relevant for cross correlations are reconstructed, we compute the projected density field by averaging the three-dimensional density field along the line of sight, i.e., the z-axis of the simulation box. Figure 3 shows the cross-correlation coefficients of the projected full dark matter density field

with the projected reconstructed density fields for the foregroud scales $k_\parallel = 0.02$ hMpc^{-1} and 0.08 hMpc^{-1}. The angular scale ℓ is related to the three-dimensional wave number k through $\ell = k\chi(z = 1)$, where $\chi(z = 1) = 2301$ Mpc$/h$ is the comoving distance to redshift $z = 1$. The cross-correlation coefficient is larger than 0.7 at scale $\ell \lesssim 100$ for the small $k_\parallel$ foreground and larger that 0.65 at scale $\ell \lesssim 100$ for the large $k_\parallel$ foreground. Therefore, the successful reconstruction of $k_\parallel \sim 0$ modes makes the cross correlation of 21-cm intensity mapping surveys with the CMB and photometric galaxy surveys possible.

IV. CROSS-CORRELATION SIGNALS

To estimate the detectibilities of the cross-correlation signals, we generate the CMB lensing convergence field, the angular galaxy distribution from photometric redshift surveys, and the temperature fluctuation due to the ISW effect from the same simulation used for tidal reconstruction. They are line of sight projections of the dark matter density field,

$$\delta_i(\boldsymbol{\theta}) = \int d\chi W_i(\chi)\delta(\chi\boldsymbol{\theta}, \chi), \qquad (15)$$

where $W_i(\chi)$ is the window function. The angular cross-correlation power spectrum is then given by

$$C_\ell^{ij} = \int d\chi \frac{W_i(\chi)W_j(\chi)}{\chi^2} P_\delta(k = \ell/\chi, \chi). \qquad (16)$$

When $i = j$, this formula gives the power spectrum for $\delta_i(\boldsymbol{\theta})$. The error for the cross-correlation signal is

$$\sigma(C_\ell^{ij}) = \left[\frac{1}{(2\ell+1)f_{\rm sky}\Delta\ell} \left((C_\ell^{ij})^2 + \hat{C}_\ell^i \hat{C}_\ell^j \right) \right]^{1/2}, \quad (17)$$

where $\hat{C}$ includes the signal and the corresponding noise. We set $\ell_{\rm min} = 12$ and choose $f_{\rm sky}$ to be 0.25 for CMB lensing and photo-z galaxies, and 1 for ISW effect.

A. CMB lensing

The lensing convergence field from CMB lensing reconstruction is a weighted projection of the dark matter density fluctuations along the line of sight to the last scattering surface,

$$\kappa(\boldsymbol{\theta}) = \int_0^{\chi_s} d\chi W_\kappa(\chi)\delta(\chi\boldsymbol{\theta}, \chi), \quad (18)$$

where the lensing kernel

$$W_\kappa(\chi) = \frac{3\Omega_{m0}H_0^2\chi(\chi_s - \chi)}{2a(\chi)\chi_s}, \quad (19)$$

and $\chi_s = \chi(z_s = 1090)$. Because the CMB lensing kernel is very broad in redshift, we take its value at redshift $z = 1$ in the line of sight projection. The noise for CMB lensing measurement is assumed to be the same as the Planck 2015 results [55].

Figure 4 shows the theoretical and measured cross power spectra. We also plot the error bars of the cross power spectrum for the $k_\parallel = 0.02 \ h{\rm Mpc}^{-1}$ foreground. Since the error bars for the $k_\parallel = 0.08 \ h{\rm Mpc}^{-1}$ foreground are just slightly larger, we only plot the error bars for the small $k_\parallel$ foreground. The total signal-to-noise ratio is 71.5 and 62.4 for the small and large $k_\parallel$ foregrounds.

B. Photo-z galaxies

We calculate the projected galaxy density field at $z \sim 1$ with usual photo-z bin width of 0.2, i.e., $z_{\rm p} \in (0.9, 1.1)$. We adopt the galaxy distribution characterized by

$$n(z) \propto z^\alpha \exp\left[-(z/z^*)^\beta \right], \quad (20)$$

with $\alpha = 2$, $z^* = 0.5$, $\beta = 1$ and assume the photometric redshift scatter $\mathcal{P}(z_{\rm p}|z)$ is perfectly known to be in a Gaussian form with photo-z rms error $\sigma_z = 0.05(1+z)$. The angular galaxy distribution is given by

$$\delta_g(\boldsymbol{\theta}) = \int_0^\infty dz W_{\rm p}(z)b(z)\delta(\chi(z)\boldsymbol{\theta}, \chi(z)), \quad (21)$$

where the window function

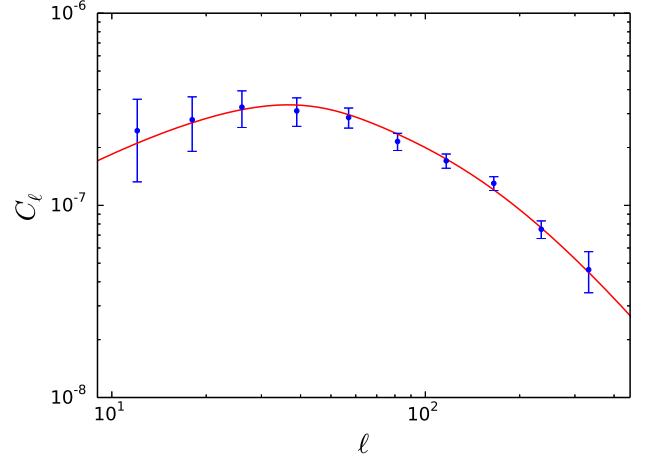$$W_{\rm p}(z) \propto n(z) \int_{0.9}^{1.1} \mathcal{P}(z_{\rm p}|z)dz_{\rm p} \quad (22)$$

FIG. 4. The cross-correlation signal of 21-cm intensity mapping and CMB lensing. The solid line shows the theoretical cross power spectrum and the data points are measured from the simulations. The error bars are for the foreground scale $R_{\rm fs} = 60 \ h/{\rm Mpc}$, i.e., $k_\parallel = 0.02 \ h{\rm Mpc}^{-1}$.
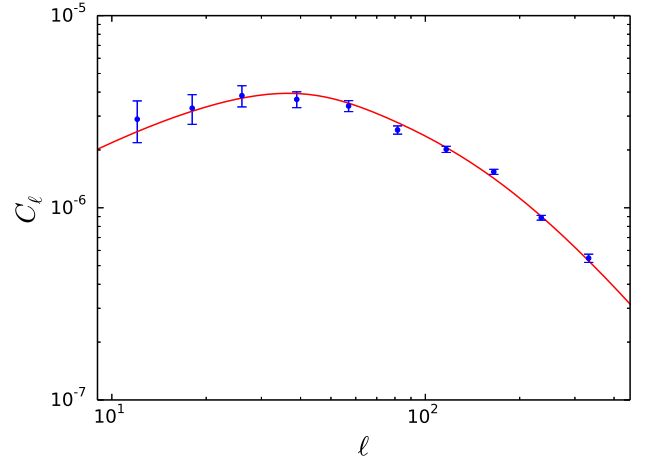

FIG. 5. The cross-correlation signal of 21-cm intensity mapping and photo-z galaxies. The solid curve shows the theoretical cross power spectrum and the data points are measured from the simulations. The error bars are for the foreground scale $R_{\rm fs} = 60 \ h/{\rm Mpc}$, i.e., $k_\parallel = 0.02 \ h{\rm Mpc}^{-1}$.

with normalization $\int W_{\rm p}(z)dz = 1$. We assume a linear galaxy bias $b(z) = 1 + 0.84z$. For photo-z galaxies from LSST-like surveys, the shot noise is negligible on degree scales.

Figure 5 shows the theoretical and measured cross power spectra. We also plot the error bars for the foregroud scale $k_\parallel = 0.02 \ h{\rm Mpc}^{-1}$. The total signal-to-noise ratio is 179.2 and 151.6 for the small and large $k_\parallel$ foregrounds, respectively. The significant cross correlation between reconstructed 21-cm field and photo-z galaxies makes it possible to calibrate the redshift distribution of galaxies from imaging surveys using 21-cm intensity mapping surveys [39].
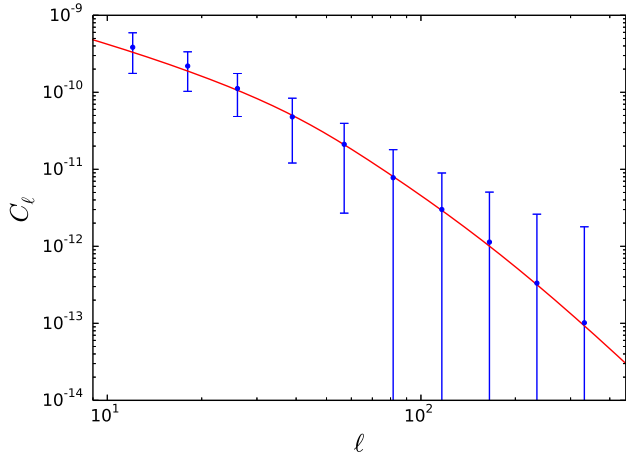
FIG. 6. The cross-correlation signal of 21-cm intensity mapping and ISW effect. The solid curve shows the theoretical signal and the data points are measured from the simulations. The error bars are for the foreground scale $R_{\rm fs} = 60~h/{\rm Mpc}$, i.e., $k_\parallel = 0.02~h{\rm Mpc}^{-1}$.

C. ISW effect

The fractional CMB temperature fluctuations induced by the ISW effect is given as

$$\left(\frac{\Delta T}{T}\right)_{\rm ISW}(\boldsymbol{\theta}) = -2 \int_0^{\chi_s} d\chi \frac{\partial \Phi(\chi\boldsymbol{\theta},\chi)}{\partial \chi} ~. \qquad (23)$$

In Fourier space, approximating that the evolution of $\delta(\boldsymbol{k},t)$ with time is given by linear theory $\dot{\delta}(\boldsymbol{k},t) = \dot{D}(t)\delta(\boldsymbol{k},t=0)$, we have

$$\frac{\partial \Phi(\boldsymbol{k},\chi)}{\partial \chi} = -\frac{3\Omega_{m0}H_0^2}{2a(\chi)} \frac{\partial \ln(D/a)}{\partial \chi} \frac{\delta(\boldsymbol{k},\chi)}{k^2} ~, \qquad (24)$$

where D is the linear growth function. In our implementation, we also approximate the time dependent factor as a constant across the simulation box. For the ISW effect, the nosie is just the large-scale CMB power C_ℓ^{TT}.

Figure 6 shows the theoretical and measured cross power spectra. We plot the error bars for the small $k_\parallel$ foreground. The total signal-to-noise ratio is 9.7 and 9.2 for the small and large $k_\parallel$ foregrounds. The redshift information from 21-cm intensity mapping allows us to constrain the expansion history of the Universe as a function of redshift. The detectability of ISW effect can be further improved by including CMB polarization data [56].

V. DISCUSSION

The detection significance presented here is for a 21-cm intenstiy mapping survey of redshifts 0.8–1.4, covering the quarter sky (full sky for ISW effect). We use line of sight projections of the dark matter density field at redshift $z = 1$ to approximate the observed cosmic fields.

In reality, we need to consider the redshift evolution of density fluctuations because of the relative wide redshift range. The Limber approximation used to compute cross power spectrum is not accurate on very large scales. Since angular power spectrum is larger when computed using exact integration than with the Limber apprximation [57, 58], the detection significance should not be degraded by this approximation. On extremely large scales, the relativistic effects should also be included when predicting the angular power spectrum [59, 60]. As there are not many modes measureable on extremely large scales, the realtivestic effects should not affect the results much. However, to be conservative, we still use only the $\ell > 12$ angular modes to estimate the detection significance.

The tidal shear estimators adopted here are optimal only for the Gaussian field and in the long wavelength limit [42, 44, 46]. The results can be improved by constructing optimal estimators for non-Gaussian fields as have done in 21-cm lensing [45]. The correlation coefficient drops quickly towards small scales. This is because there is not enough small-scale modes in 21-cm intensity mapping surveys and the estimators are not optimal in the equalateral configuration. The long wavelength optimal estimators relies on the number of small-scale modes; the performance would be better with more small-scale structures. The tidal reconstruction can still be improved by developing new algorithms to deal with the nonlinear coupling beyond the squeezed configuration.

The BAO reconstruction technique has been shown to be still useful in 21-cm surveys [61–63]. While there are not many mode with small $k_\parallel$ lost due to the foreground, the differential motions which smear the BAO peak are substantially contributed by large-scale modes with $k \lesssim 0.1~h{\rm Mpc}^{-1}$. Performing nonlinear reconstruction also needs these modes to estimate the large-scale linear displacement [47, 64, 65]. Cosmic tidal reconstruction compensates the foreground wedge at small $k_\parallel$ and large $k_\perp$ and hence can improve the BAO measurements from 21-cm surveys [61, 62]. These recovered foreground modes can also improve the efficiency of the void finder with interferometric 21-cm experiments [52]. In addition to the cross correlations explored here, the tidal reconstruction method also works for the kinematic Sunyaev-Zel'dovich effect which we leave for future work.

All cosmological 21-cm experiments share the same foreground problem, no matter low redshift BAO experiment or high redshift epoch of reionization observation. Therefore, the tidal reconstruction method is also important for high redshift experiment such as measuring the cross correlation of 21-cm with the kinematic Sunyaev-Zel'dovich effect from the epoch of reionization [66].

---

[1] S. Alam, M. Ata, S. Bailey, F. Beutler, D. Bizyaev, J. A. Blazek, A. S. Bolton, J. R. Brownstein, A. Burden, C.-H. Chuang, et al., Mon. Not. R. Astron. Soc. **470**, 2617 (2017), 1607.03155.

[2] Dark Energy Survey Collaboration, T. Abbott, F. B. Abdalla, J. Aleksić, S. Allam, A. Amara, D. Bacon, E. Balbinot, M. Banerji, K. Bechtol, et al., Mon. Not. R. Astron. Soc. **460**, 1270 (2016), 1601.00329.

[3] M. Takada, R. S. Ellis, M. Chiba, J. E. Greene, H. Aihara, N. Arimoto, K. Bundy, J. Cohen, O. Doré, G. Graves, et al., Publ. Astron. Soc. Jpn. **66**, R1 (2014), 1206.0737.

[4] DESI Collaboration, A. Aghamousa, J. Aguilar, S. Ahlen, S. Alam, L. E. Allen, C. Allende Prieto, J. Annis, S. Bailey, C. Balland, et al., ArXiv e-prints (2016), 1611.00036.

[5] LSST Science Collaboration, P. A. Abell, J. Allison, S. F. Anderson, J. R. Andrew, J. R. P. Angel, L. Armus, D. Arnett, S. J. Asztalos, T. S. Axelrod, et al., ArXiv e-prints (2009), 0912.0201.

[6] L. Amendola, S. Appleby, D. Bacon, T. Baker, M. Baldi, N. Bartolo, A. Blanchard, C. Bonvin, S. Borgani, E. Branchini, et al., Living Reviews in Relativity **16**, 6 (2013), 1206.1225.

[7] Planck Collaboration, R. Adam, P. A. R. Ade, N. Aghanim, Y. Akrami, M. I. R. Alves, F. Argüeso, M. Arnaud, F. Arroja, M. Ashdown, et al., A&A **594**, A1 (2016), 1502.01582.

[8] B. A. Benson, P. A. R. Ade, Z. Ahmed, S. W. Allen, K. Arnold, J. E. Austermann, A. N. Bender, L. E. Bleem, J. E. Carlstrom, C. L. Chang, et al., in *Millimeter, Submillimeter, and Far-Infrared Detectors and Instrumentation for Astronomy VII* (2014), vol. 9153 of Proc. SPIE, p. 91531P, 1407.2973.

[9] S. W. Henderson, R. Allison, J. Austermann, T. Baildon, N. Battaglia, J. A. Beall, D. Becker, F. De Bernardis, J. R. Bond, E. Calabrese, et al., Journal of Low Temperature Physics **184**, 772 (2016), 1510.02809.

[10] K. N. Abazajian, P. Adshead, Z. Ahmed, S. W. Allen, D. Alonso, K. S. Arnold, C. Baccigalupi, J. G. Bartlett, N. Battaglia, B. A. Benson, et al., ArXiv e-prints (2016), 1610.02743.

[11] T.-C. Chang, U.-L. Pen, J. B. Peterson, and P. McDonald, Phys. Rev. Lett. **100**, 091303 (2008), 0709.3672.

[12] A. Loeb and J. S. B. Wyithe, Phys. Rev. Lett. **100**, 161301 (2008), 0801.1677.

[13] H.-J. Seo, S. Dodelson, J. Marriner, D. Mcginnis, A. Stebbins, C. Stoughton, and A. Vallinotto, Astrophys. J. **721**, 164 (2010), 0910.5007.

[14] K. Bandura et al., in *Society of Photo-Optical Instrumentation Engineers (SPIE) Conference Series* (2014), vol. 9145 of *Society of Photo-Optical Instrumentation Engineers (SPIE) Conference Series*, p. 22, 1406.2288.

[15] L. B. Newburgh, K. Bandura, M. A. Bucher, T.-C. Chang, H. C. Chiang, J. F. Cliche, R. Davé, M. Dobbs, C. Clarkson, K. M. Ganga, et al., in *Ground-based and Airborne Telescopes VI* (2016), vol. 9906 of Proc. SPIE, p. 99065X, 1607.02059.

[16] Y. Xu, X. Wang, and X. Chen, Astrophys. J. **798**, 40 (2015), 1410.7794.

[17] R. A. Battye, I. W. A. Browne, C. Dickinson, G. Heron, B. Maffei, and A. Pourtsidou, Mon. Not. R. Astron. Soc. **434**, 1239 (2013), 1209.0343.

[18] M.-A. Bigot-Sazy, Y.-Z. Ma, R. A. Battye, I. W. A. Browne, T. Chen, C. Dickinson, S. Harper, B. Maffei, L. C. Olivari, and P. N. Wilkinsondagger, in *Frontiers in Radio Astronomy and FAST Early Sciences Symposium 2015*, edited by L. Qain and D. Li (2016), vol. 502 of *Astronomical Society of the Pacific Conference Series*, p. 41, 1511.03006.

[19] M. G. Santos, M. Cluver, M. Hilton, M. Jarvis, G. I. G. Jozsa, L. Leeuw, O. Smirnov, R. Taylor, F. Abdalla, J. Afonso, et al., ArXiv e-prints (2017), 1709.06099.

[20] M. Santos, P. Bull, D. Alonso, S. Camera, P. Ferreira, G. Bernardi, R. Maartens, M. Viel, F. Villaescusa-Navarro, F. B. Abdalla, et al., Advancing Astrophysics with the Square Kilometre Array (AASKA14) 19 (2015), 1501.03989.

[21] S. P. Oh and K. J. Mack, Mon. Not. R. Astron. Soc. **346**, 871 (2003), astro-ph/0302099.

[22] S. R. Furlanetto, S. P. Oh, and F. H. Briggs, Phys. Rep. **433**, 181 (2006), astro-ph/0608032.

[23] A. Datta, J. D. Bowman, and C. L. Carilli, Astrophys. J. **724**, 526 (2010), 1005.4071.

[24] M. F. Morales, B. Hazelton, I. Sullivan, and A. Beardsley, Astrophys. J. **752**, 137 (2012), 1202.3830.

[25] H. Vedantham, N. Udaya Shankar, and R. Subrahmanyan, Astrophys. J. **745**, 176 (2012), 1106.1297.

[26] J. C. Pober, A. R. Parsons, J. E. Aguirre, Z. Ali, R. F. Bradley, C. L. Carilli, D. DeBoer, M. Dexter, N. E. Gugliucci, D. C. Jacobs, et al., ApJ **768**, L36 (2013), 1301.7099.

[27] J. C. Pober, Mon. Not. R. Astron. Soc. **447**, 1705 (2015), 1411.2050.

[28] A. Liu and M. Tegmark, Phys. Rev. D **83**, 103006 (2011), 1103.0281.

[29] A. Liu and M. Tegmark, Mon. Not. R. Astron. Soc. **419**, 3491 (2012), 1106.0007.

[30] J. R. Shaw, K. Sigurdson, U.-L. Pen, A. Stebbins, and M. Sitwell, Astrophys. J. **781**, 57 (2014), 1302.0327.

[31] J. R. Shaw, K. Sigurdson, M. Sitwell, A. Stebbins, and U.-L. Pen, Phys. Rev. D **91**, 083514 (2015), 1401.2095.

[32] D. Kirk, F. B. Abdalla, A. Benoit-Lévy, P. Bull, and B. Joachimi, Advancing Astrophysics with the Square Kilometre Array (AASKA14) 20 (2015), 1501.03848.

[33] A. Pourtsidou, D. Bacon, R. Crittenden, and R. B. Metcalf, Mon. Not. R. Astron. Soc. **459**, 863 (2016), 1509.03286.

[34] A. Pourtsidou, Mon. Not. R. Astron. Soc. **461**, 1457 (2016), 1511.05927.

[35] D. Alonso and P. G. Ferreira, Phys. Rev. D **92**, 063525 (2015), 1507.03550.

[36] J. Fonseca, S. Camera, M. G. Santos, and R. Maartens, ApJ **812**, L22 (2015), 1507.04605.

[37] J. Fonseca, R. Maartens, and M. G. Santos, Mon. Not. R. Astron. Soc. **466**, 2780 (2017), 1611.01322.

[38] A. Pourtsidou, D. Bacon, and R. Crittenden, Mon. Not. R. Astron. Soc. **470**, 4251 (2017), 1610.04189.

[39] D. Alonso, P. G. Ferreira, M. J. Jarvis, and K. Moodley, Phys. Rev. D **96**, 043515 (2017), 1704.01941.

[40] U. Seljak, Phys. Rev. Lett. **102**, 021302 (2009), 0807.1770.

[41] U.-L. Pen, R. Sheth, J. Harnois-Deraps, X. Chen, and Z. Li, ArXiv e-prints (2012), 1202.5804.

[42] H.-M. Zhu, U.-L. Pen, Y. Yu, X. Er, and X. Chen, Phys. Rev. D **93**, 103504 (2016), 1511.04680.

[43] F. Schmidt, E. Pajer, and M. Zaldarriaga, Phys. Rev. D **89**, 083507 (2014), 1312.5616.

[44] T. Lu and U.-L. Pen, Mon. Not. R. Astron. Soc. **388**, 1819 (2008), 0710.1108.

[45] T. Lu, U.-L. Pen, and O. Doré, Phys. Rev. D **81**, 123015 (2010), 0905.0499.

[46] M. Bucher, C. S. Carvalho, K. Moodley, and M. Remazeilles, Phys. Rev. D **85**, 043016 (2012), 1004.3285.

[47] H.-M. Zhu, Y. Yu, and U.-L. Pen, ArXiv e-prints (2017), 1711.03218.

[48] U. Seljak, G. Aslanyan, Y. Feng, and C. Modi, J. Cosmology Astropart. Phys. **12**, 009 (2017), 1706.06645.

[49] M. Schmittfull, T. Baldauf, and M. Zaldarriaga, Phys. Rev. D **96**, 023505 (2017), 1704.06634.

[50] J. Harnois-Déraps, U.-L. Pen, I. T. Iliev, H. Merz, J. D. Emberson, and V. Desjacques, Mon. Not. R. Astron. Soc. **436**, 540 (2013), 1208.5098.

[51] E. Castorina and F. Villaescusa-Navarro, Mon. Not. R. Astron. Soc. **471**, 1788 (2017), 1609.05157.

[52] M. White and N. Padmanabhan, Mon. Not. R. Astron. Soc. **471**, 1167 (2017), 1705.09669.

[53] K. W. Masui, E. R. Switzer, N. Banavar, K. Bandura, C. Blake, L.-M. Calin, T.-C. Chang, X. Chen, Y.-C. Li, Y.-W. Liao, et al., ApJ **763**, L20 (2013), 1208.0331.

[54] E. R. Switzer, K. W. Masui, K. Bandura, L.-M. Calin, T.-C. Chang, X.-L. Chen, Y.-C. Li, Y.-W. Liao, A. Natarajan, U.-L. Pen, et al., Mon. Not. R. Astron. Soc. **434**, L46 (2013), 1304.3712.

[55] Planck Collaboration, P. A. R. Ade, N. Aghanim, M. Arnaud, M. Ashdown, J. Aumont, C. Baccigalupi, A. J. Banday, R. B. Barreiro, J. G. Bartlett, et al., A&A **594**, A15 (2016), 1502.01591.

[56] G.-C. Liu, K.-W. Ng, and U.-L. Pen, Phys. Rev. D **83**, 063001 (2011), 1010.0578.

[57] V. Assassi, M. Simonović, and M. Zaldarriaga, J. Cosmology Astropart. Phys. **11**, 054 (2017), 1705.05022.

[58] M. Schmittfull and U. Seljak, ArXiv e-prints (2017), 1710.09465.

[59] A. Hall, C. Bonvin, and A. Challinor, Phys. Rev. D **87**, 064026 (2013), 1212.0728.

[60] A. Hall and C. Bonvin, Phys. Rev. D **95**, 043530 (2017), 1609.09252.

[61] H.-J. Seo and C. M. Hirata, Mon. Not. R. Astron. Soc. **456**, 3142 (2016), 1508.06503.

[62] J. D. Cohn, M. White, T.-C. Chang, G. Holder, N. Padmanabhan, and O. Doré, Mon. Not. R. Astron. Soc. **457**, 2068 (2016), 1511.07377.

[63] A. Obuljen, F. Villaescusa-Navarro, E. Castorina, and M. Viel, J. Cosmology Astropart. Phys. **9**, 012 (2017), 1610.05768.

[64] H.-M. Zhu, U.-L. Pen, and X. Chen, ArXiv e-prints (2016), 1609.07041.

[65] H.-M. Zhu, Y. Yu, U.-L. Pen, X. Chen, and H.-R. Yu, Phys. Rev. D **96**, 123502 (2017), 1611.09638.

[66] M. A. Alvarez, Astrophys. J. **824**, 118 (2016), 1511.02846.